



## Original Article

# Three-D core multiphysics for simulating passively autonomous power maneuvering in soluble-boron-free SMR with helical steam generator

Ahmed Amin E. Abdelhameed, Khurram Saleem Chaudri<sup>1</sup>, Yonghee Kim<sup>\*</sup>

Department of Nuclear & Quantum Engineering, Korea Advanced Institute of Science and Technology, 291 Daehak-ro Yuseong-gu, Daejeon, 34141, South Korea

## ARTICLE INFO

## Article history:

Received 6 February 2020

Received in revised form

3 May 2020

Accepted 11 May 2020

Available online 16 May 2020

## Keywords:

Helical-coil steam generator

SMR

Passively autonomous power maneuvering

Coolant temperature coefficient

Soluble-boron-free PWR

Reactivity feedback

Predictor-corrector quasi-static

## ABSTRACT

Helical-coil steam generator (HCSG) technology is a major design candidate for small modular reactors due to its compactness and capability to produce superheated steam with high generation efficiency. In this paper, we investigate the feasibility of the passively autonomous power maneuvering by coupling the 3-D transient multi-physics of a soluble-boron-free (SBF) core with a time-dependent HCSG model. The predictor corrector quasi-static method was used to reduce the cost of the transient 3-D neutronic solution. In the numerical system simulations, the feedwater flow rate to the secondary of the HCSGs is adjusted to extract the demanded power from the primary loop. This varies the coolant temperature at the inlet of the SBF core, which governs the passively autonomous power maneuvering due to the strongly negative coolant reactivity feedback. Here, we simulate a 100-50-100 load-follow operation with a 5%/minute power ramping speed to investigate the feasibility of the passively autonomous load-follow in a 450 MW<sub>th</sub> SBF PWR. In addition, the passively autonomous frequency control operation is investigated. The various system models are coupled, and they are solved by an in-house Fortran-95 code. The results of this work demonstrate constant steam temperature in the secondary side and limited variation of the primary coolant temperature. Meanwhile, the variations of the core axial shape index and the core power peaking are sufficiently small.

© 2020 Korean Nuclear Society, Published by Elsevier Korea LLC. This is an open access article under the CC BY-NC-ND license (<http://creativecommons.org/licenses/by-nc-nd/4.0/>).

## 1. Introduction

In the conventional pressurized water reactors (PWRs), the coolant temperature is programmed with power. For example, constant inlet coolant temperature ( $T_i$ ) with power is used in the Korean OPR1000 reactor. However, in the French and German PWRs,  $T_i$  varies with power [1]. In the conventional designs, the control rods (CRs) are responsible for maintaining the programmed coolant temperature and axial shape index (ASI) [2–4] during a power maneuvering. However, in the passively autonomous frequency control operation (PAFO) [5] and the passively autonomous load-follow (PLFO), the variation of  $T_i$  compensates largely for the reactivity changes during the power maneuvering. Favorable

conditions for these new operational schemes can be attained in a soluble-boron-free (SBF) small modular reactor (SMR). This is mainly due to the strongly negative coolant temperature coefficient (CTC) from the beginning of the cycle (BOC) [5,6]. In a previous work [7], we illustrated the feasibility of PAFO in the SBF ATOM SMR by coupling the 3-D core multi-physics with a simplified steam generator (SG) model. In that simplified SG model, the thermal-hydraulic solution was obtained by solving the conservation equations only in the primary loop and setting the amount of power transferred to the secondary loop to be equal to the time-dependent variation of the power demand. This model cannot provide any information regarding the secondary side. However, quantifying the variation of the steam temperature in the secondary loop and the required variation of feedwater flow rate to the secondary side of the SG are important quantities to demonstrate the feasibility of the newly proposed operational modes.

Upon this motivation, in this paper, we couple our previously developed in-house 3-D core multi-physics code with an in-house module that solves a time-dependent helical-coil steam generator

<sup>\*</sup> Corresponding author.

E-mail address: [yongheekim@kaist.ac.kr](mailto:yongheekim@kaist.ac.kr) (Y. Kim).

<sup>1</sup> Permanent Address: Department of Nuclear Engineering, Pakistan Institute of Engineering and Applied Sciences (PIEAS), Nilore 45,650 Islamabad.

(HCSG) model. The new module provides the thermal-hydraulic solution in both the primary and secondary loops of the HCSG. The solution is obtained based on coolant conditions and a known feedwater flow rate to the secondary side of the HCSG that is proportional to the power demand variation. Meanwhile, the time-dependent variation of the primary side inlet of the HCSG is obtained from the core thermal-hydraulic analysis and the time-delay on the core hot leg. Fig. 1 provides a demonstration of the system model in which the core model is coupled with an HCSG model. Dynamic responses of the SMR system are analyzed by an in-house Fortran-95 computer program.

## 2. Models and methodologies

### 2.1. 3-D dynamic multi-physics and predictor-corrector quasi-static scheme

The neutronic modelling and analysis are based on the typical two-step procedure for light water reactors. In this study, group-wise cross-sections and transient parameters are obtained by Monte Carlo simulations using the Serpent-2 code [8] with the ENDF/B-VII7.1 data library. Meanwhile, the nodal expansion method (NEM) [9] with assembly discontinuity factor (ADF) is used for the whole core calculations. The neutronic solution is coupled with a time-dependent thermal-hydraulic (TH) module which comprises core thermal analysis for all fuel assemblies. Fig. 2 represents the algorithm of the core multi-physics simulation.

The predictor-corrector quasi-static method (PCQM) [10,11] is implemented to reduce the computational cost of the dynamic nodal solution. In PCQM, the neutron flux is factorized to its shape and amplitude parts. The neutron shape is first predicted from the transient fixed source nodal solution for a relatively large time interval, which is referred to as a macro time step. The predicted shape function is used to obtain the point kinetic (PK) parameters for the macro step. Then, the PK equation is solved with a smaller time step, so-called micro time step, to correct the amplitude of the neutron flux. The algorithm of the multi-physics solution with the

PCQM is shown in Fig. 3. It is worthwhile to mention that the time-dependent TH and Xe calculations are relatively inexpensive, in comparison with the 3-D time-dependent nodal solution, therefore, we update them on the micro time step.

The time-dependent neutron diffusion equation can be written in the form in Eq. (1). The factorization of the neutron flux to a shape function  $\psi(r,E,t)$  and amplitude function  $p(t)$  is given in Eq. (2). By making use of Eq. (2) and multiplying Eq. (1), and the delayed neutron precursors balance equation, by a weighting function  $w(r,E)$  then performing integration over the space and the energy, the solution can be lumped in the PK form given in Eq. (3). The amplitude attained from Eq. (3) is then used to obtain a corrected flux  $\phi(r,E,t)$ , as given in Eq. (4). In this equation,  $N(t)$  is a normalization factor.

$$L\phi_g(t) + R\phi_g(t) + \frac{\partial\phi_g(t)}{\nu_g\partial t} = \frac{\chi_{pg}}{k_0}(1-\beta)F\phi_g(t) + S\phi_g(t) + \sum_{k=1}^6 S_k(t). \quad (1)$$

where

$$\begin{aligned} L\phi_g(t) &= -\nabla \cdot D_g(t) \nabla \phi_g(t), \\ R\phi_g(t) &= \Sigma_{r,g}(t) \phi_g(t), \\ S\phi_g(t) &= \sum_{g' \neq g} \Sigma_{s,g' \rightarrow g}(t) \phi_{g'}(t), \\ F\phi_g(t) &= \sum_{g'=1}^G \nu_{g'} \Sigma_{f,g'}(t) \phi_{g'}(t), \\ S_k(t) &= \chi_{k,g} \lambda_k C_k(t). \end{aligned} \quad (2)$$

$$\phi(r, E, t) = p(t) \psi(r, E, t).$$

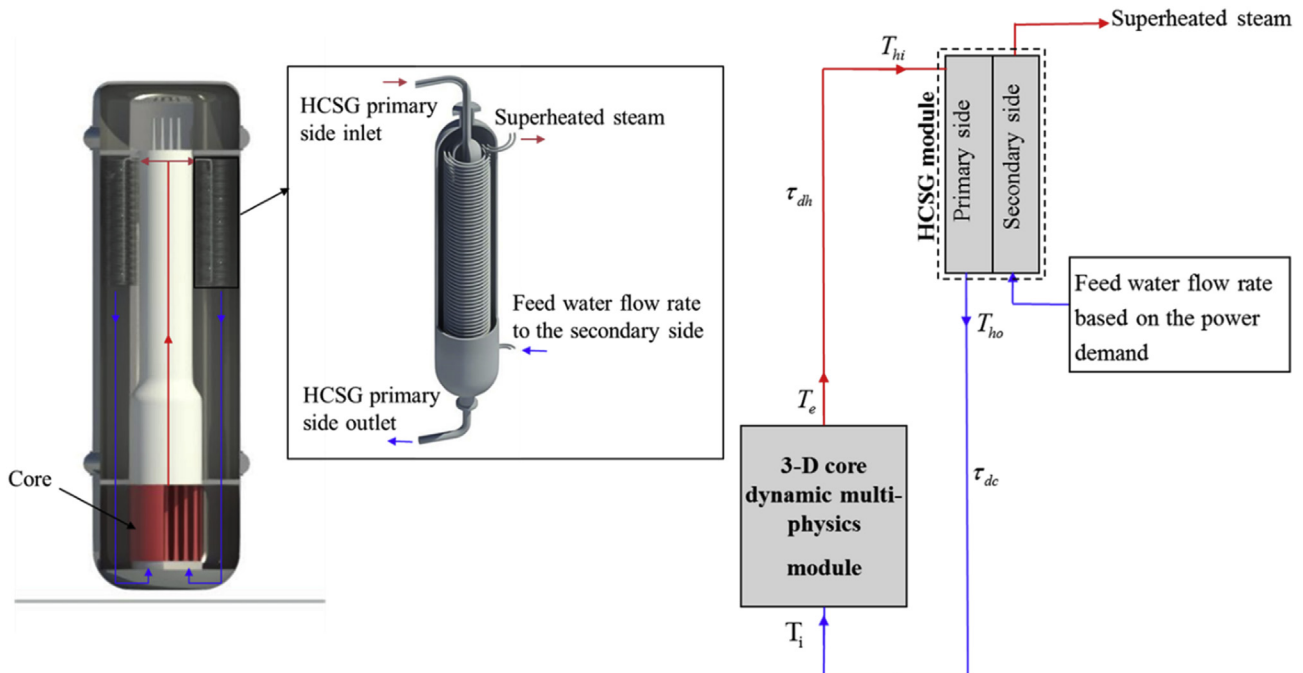


Fig. 1. Schematics of the system model.

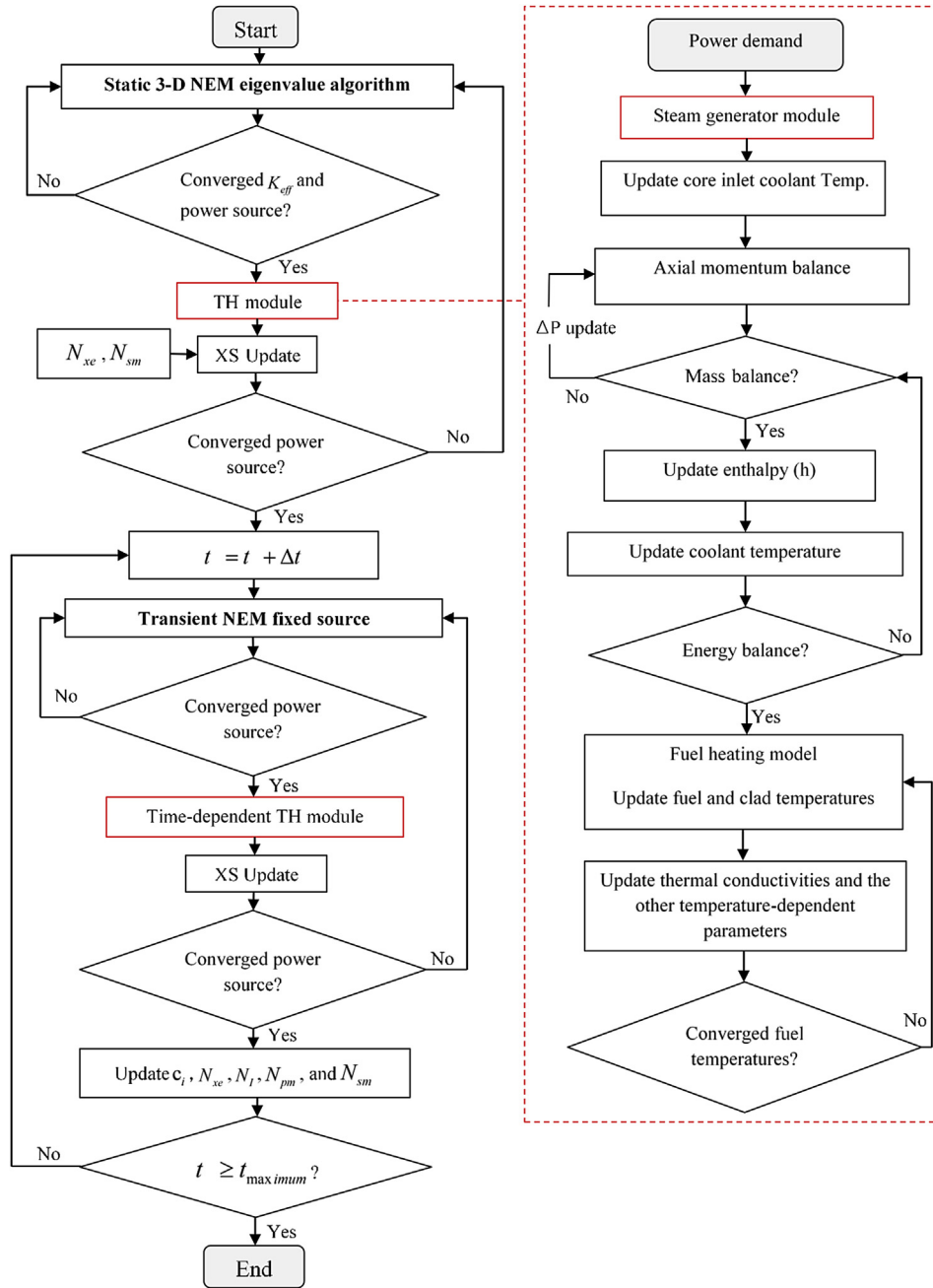


Fig. 2. Algorithm of the multi-physics core analysis.

$$\frac{dp(t)}{dt} = \frac{\rho(t) - \beta(t)}{\Lambda} p(t) + \sum_k \lambda_k C_k(t),$$

$$\frac{dC_k(t)}{dt} = -\lambda_k C_k(t) + \frac{\beta_k}{\Lambda} p(t), k = 1, 2, \dots, 6,$$

where

(3)

$$\rho(t) = 1 - \frac{K_0}{K(t)},$$

$$K(t) = \frac{\langle w(r, E), \chi_P(E) F \Psi(r, E, t) \rangle}{\langle w(r, E), (L + R - S) \Psi(r, E, t) \rangle},$$

$$\beta_k(t) = \frac{\langle w(r, E), \chi_k(E) \beta_k F \Psi(r, E, t) \rangle}{\langle w(r, E), \chi_P(E) F \Psi(r, E, t) \rangle},$$

$$\Lambda(t) = \frac{\langle w(r, E), \frac{1}{v(E)} \Psi(r, E, t) \rangle}{\langle w(r, E), \frac{1}{K_0} \chi_P(E) F \Psi(r, E, t) \rangle}.$$

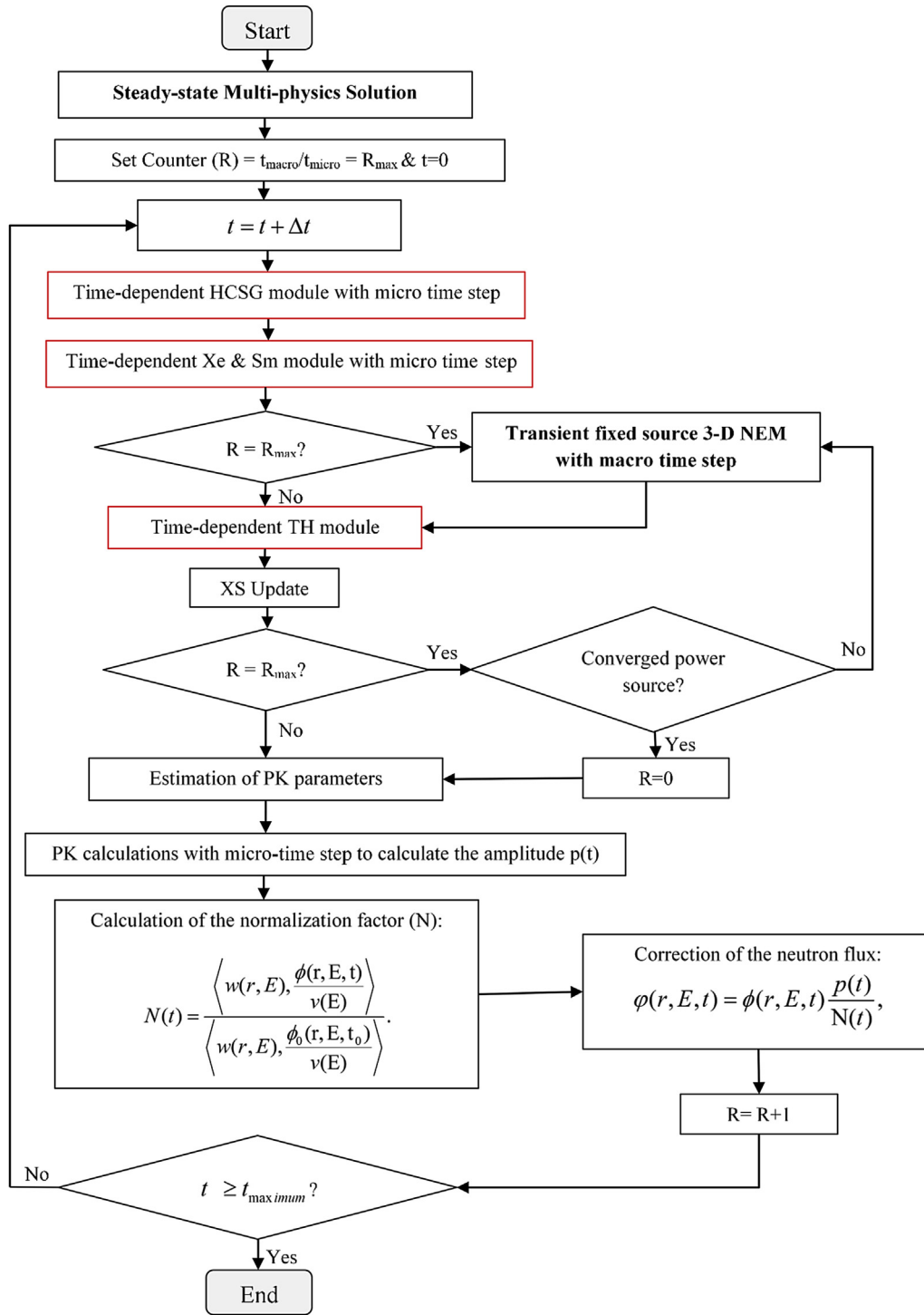


Fig. 3. PCQM algorithm in the in-house 3D system code.

$$\varphi(r, E, t) = \varphi(r, E, t) \frac{p(t)}{N(t)}, \quad (4)$$

where

$$N(t) = \frac{\langle w(r, E), \frac{\phi(r, E, t)}{v(E)} \rangle}{\langle w(r, E), \frac{\phi_0(r, E, t_0)}{v(E)} \rangle}.$$

In order to test the accurate implementation of the PCQM for the 3-D multi-physics analysis, the ATOM core was simulated by the 3-D NEM code coupled with the whole core TH analysis and an SG model. The power demand was assumed to vary rapidly with 0.5% of the rated power per second. In the PCQM, the PK solution was estimated with 0.1 s time-step and the neutron balance was solved with various time-steps: 0.1 s, 0.4 s, and 0.8 s. The PCQM solutions are compared with the direct 3-D NEM dynamic solution that is solved with a 0.1 s time-step. Good agreement between the PCQM

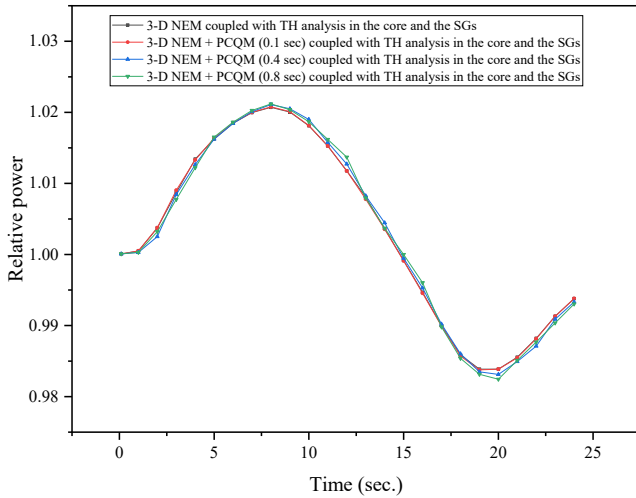


Fig. 4. Comparison of PCQM solutions with direct nodal solution.

solutions and the reference one is confirmed as illustrated in Fig. 4.

## 2.2. Helical-coil SG model

A TH model has been developed to calculate the steady and transient thermal-hydraulics characteristics of the HCSG, and it is coupled with the 3-D core multi-physics code. In the numerical simulations, the secondary feedwater flow rate is adjusted, proportionally to the power demand variation, to extract the required energy from the primary loop. The single-channel methodology is used, i.e., no crossflow is considered. Therefore, the basic governing balance equations of mass, energy, and axial momentum can be written as shown in Eq. (5), Eq. (6), and Eq. (7), respectively [12]. In the equations, subscript  $i$  stands for the axial node index and  $m$  is the axial mass flow rate,  $A$  is the flow area,  $\rho$  is the density,  $\Delta z$  is the node's height,  $q'$  is the linear power generation,  $h$  is the enthalpy, and  $v$  is the flow velocity. In addition, the pressure is denoted as  $P$ , the gravitational acceleration is denoted as  $g$ , and  $F$  indicates the summation of the forces acting on the node that causes pressure drop by wall friction and form drag. It should be noted that no heat generation in the fluid is considered. The heat dissipation, due to viscous effects, is considered negligible. In addition, axial heat conduction in the fluid is ignored.

In the HCSG module, the solution of the conservation equations is obtained in a similar manner that is described in Refs. [7]. After getting a converged temperature profile for the coolant, surface heat transfer routine is carried out to calculate the heat transfer coefficient. Then, the secondary side thermal-hydraulics calculations are performed.

The thermal-hydraulics solutions for both primary and secondary sides are performed based on known power demand and

flow rates. For the first iteration, the power profile is assumed to be constant over the whole length. For the following iterations, the solution for both the primary and the secondary sides of the HCSG is used to calculate a new power profile using equation Eq. (8). In Eq. (8),  $Q_i$  is the power of an axial node  $i$ , and the subscripts pr, and sc stand for related quantities to the primary side and the secondary sides, respectively. Meanwhile,  $T$  and  $H$  stand for the coolant temperature and the heat transfer coefficient, respectively.  $A_{pr}$  is the heat transfer area of the primary side, and  $A_{sc}$  is the heat transfer area of the secondary side,  $A_t$  is the tube area,  $\tau$  is the tube thickness, and  $K_t$  is the tube thermal conductivity. This power profile is then compared to the previous iteration power profile. Until a converged solution is obtained for the power profile, the newly obtained power profile is used to perform thermal-hydraulic calculations for both the primary and secondary sides of the HCSG. Fig. 5 illustrates the HCSG module algorithm.

In the homogenous two-phase mixture model, thermodynamic equilibrium is considered between liquid and vapor phases, i.e., equal temperature and equal velocity for both phases. In such a model, the vapor mass fraction in the two-phase mixture or the thermodynamic quality ( $x_v$ ) is given by Eq. (9). In Eq. (9),  $h_{mix}$  is the mixture enthalpy,  $h_{sl}$  is the enthalpy of the saturated liquid, and  $h_{sv}$  is the enthalpy of the saturated vapor. Meanwhile, in order to improve the homogeneous model, thermal equilibrium conditions are improved by computing the flow quality that is the equivalent bulk quality ( $x$ ) in Eqs. 10 and 11 [13]. In the equations,  $x_d$  is the bubble departure quality. Meanwhile, in a similar manner to that used in COBRA-EN [13],  $x_d$  is determined by utilizing an empirical function ( $Z$ ) in Eq. (12).  $C_{pl}$  is the specific heat of the subcooled liquid and  $h_{lg}$  is the latent vaporization heat ( $h_{sg} - h_{sl}$ ). Equations 13–19 are used for determining  $Z$ . In these equations, the subscript “l” stands for a liquid state quantity. Reynold and Prandtl numbers are denoted as  $Re$  and  $Pr$ , respectively.  $D_h$  is the hydraulic diameter,  $K$  is the thermal conductivity, and  $P$  is the pressure. These equations use quantities in AE system of units. Thus, relevant conversion factors were applied in the HCSG module. After the flow-quality is obtained, Armand-Massena correlation is used to obtain the void fraction for the flow conditions.

In order to obtain the values of the heat transfer coefficient, various correlations are included in the code according to the flow conditions. For liquid and fully gas convective heat transfer, the Dittus-Boelter correlation is used as given in Eq. (19). Subcooled and saturated nucleate boiling heat transfer is calculated using Thom's correlation in Eq. (20) plus liquid phase forced convection calculated by making use of the Dittus-Boelter correlation for a turbulent flow condition, as shown in Eq. (21). The transition from single-phase liquid forced convection to onset of nucleate boiling is determined based on the quality value. For a quality value of zero or one, i.e., fully liquid or fully vapor (gas) single-phase case, Dittus-Boelter heat transfer is used. For a quality value between zero and one, Dittus plus Thom correlations are used for calculating the heat transfer correlation. For single-phase friction factor ( $f$ ), the selection is done based on  $Re$ , as shown in Eq. (22) – (24).

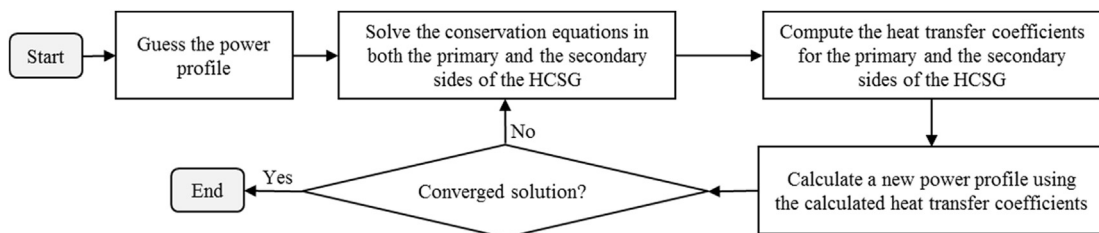
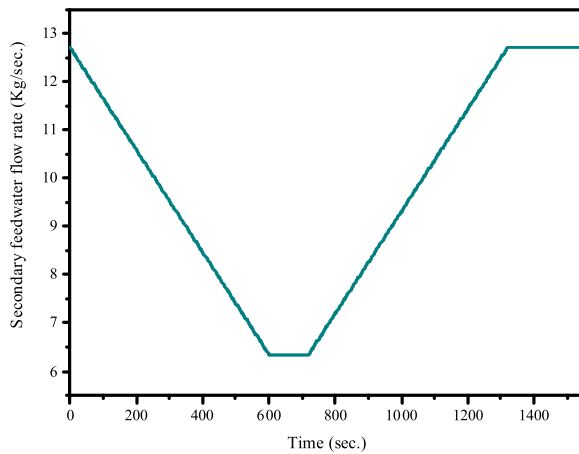


Fig. 5. The helical-coil steam generator algorithm.

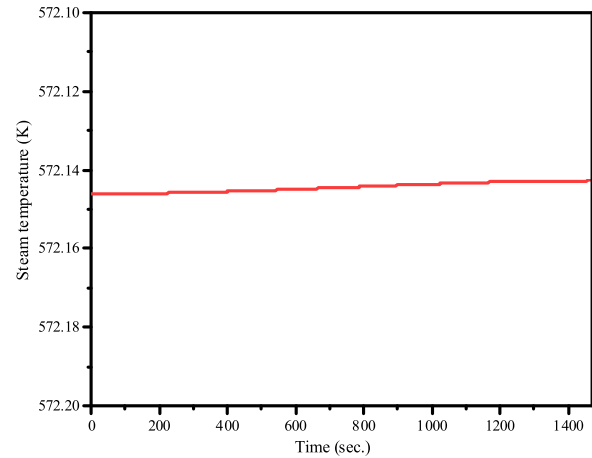
**Table 1**

Major parameters for the ATOM core and helical-coil steam generator.

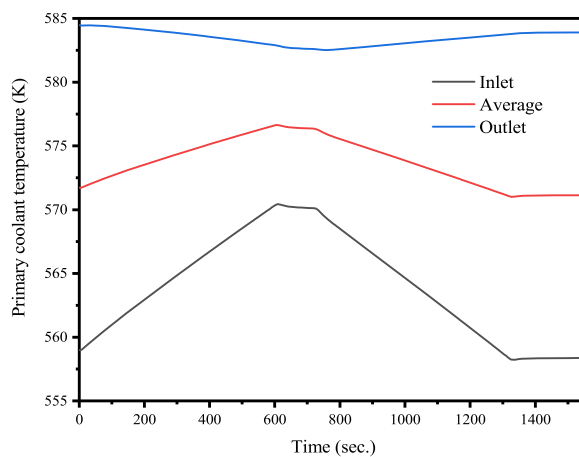
Parameter	Value (unit)
Core	
Thermal power (MWth)	450
Active core height (cm)	200
Equivalent diameter (cm)	201.6
Number of fuel assemblies	69
Fuel assembly design	17 × 17
Fuel enrichment (w/o)	5
Cycle length (months)	38
Steam Generator	
Primary pressure (bar)	150
Secondary pressure (bar)	34
Number of SGs	16
Number of tubes/SG	324
Primary flow rate/SG (kg/sec)	202
Secondary flow rate/SG (kg/sec)	12.7
SG Primary inlet temperature (K)	584.5
SG secondary inlet temperature (K)	453
Primary axial height (m)	2.8
Secondary tube length (m)	15.8
Tube inner diameter (mm)	9
Tube outer diameter (mm)	12
Innermost coil diameter (m)	0.182



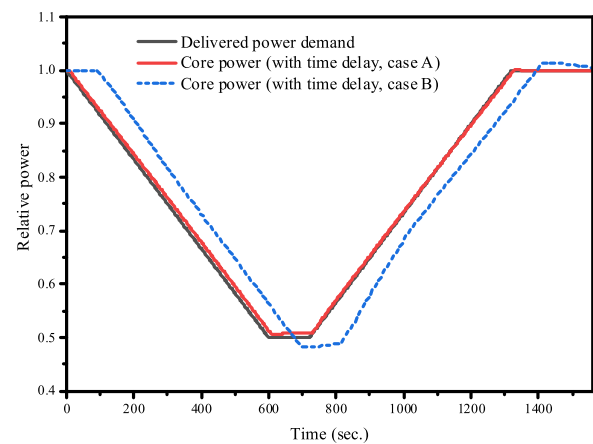
a. Secondary feed water flow adjustment



c. Steam temperature in the secondary side



b. Core coolant temperatures



d. Core power and power demand

**Fig. 6.** PLFO simulation performed by 3-D core multi-physics coupled with HCSG module.



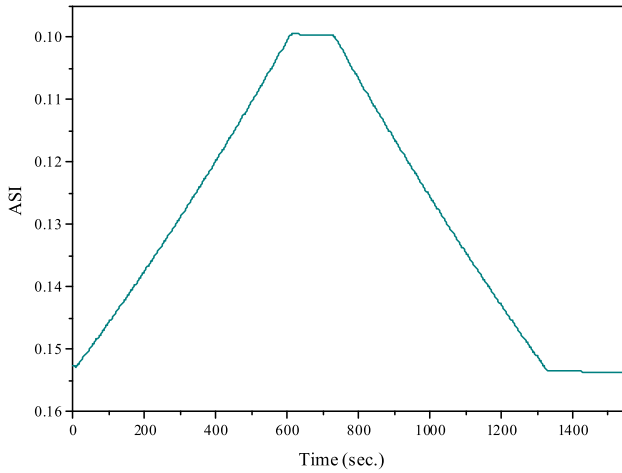
Meanwhile, for the two-phase friction multiplier ( $\zeta^2$ ), Armand correlation is used in the TH module as given in Eqs. 25–27 [13]. In the equations,  $\alpha$  is the void fraction and it is estimated using Armand-Massena correlation in Eq. (28), where  $R$  is the ratio of the specific volumes of liquid and vapor.

$$A_i \frac{\partial \rho_i}{\partial t} + \frac{\Delta m_i}{\Delta z_i} = 0, \quad (5)$$

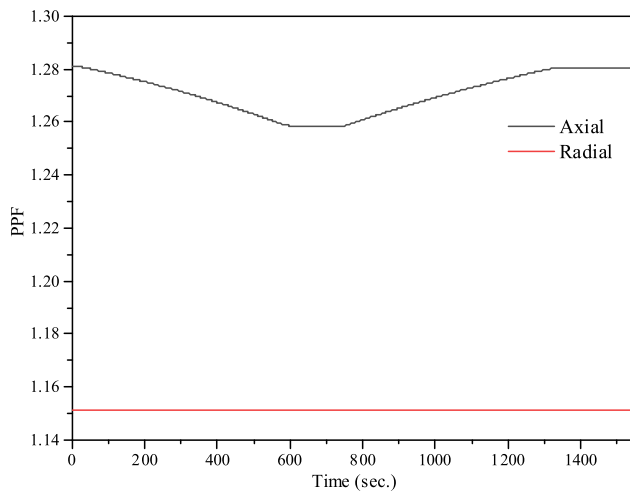
$$A_i \frac{\partial (\rho_i h_i)}{\partial t} + \frac{\Delta (m_i h_i)}{\Delta z_i} = q'_i, \quad (6)$$

$$\frac{\partial m_i}{\partial t} + \frac{\Delta (m_i v_i)}{\Delta z_i} = -A_i \rho_i g_i - A_i \frac{\Delta P_i}{\Delta z_i} - \frac{F_i}{\Delta z_i}, \quad (7)$$

$$Q_i = \frac{T_{pr,i} - T_{sc,i}}{\left( \frac{1}{H_{pr,i} A_{pr,i}} \right) + \left( \frac{1}{H_{sc,i} A_{sc,i}} \right) + \left( \frac{\tau}{K_{t,i} A_{t,i}} \right)}. \quad (8)$$



a. ASI



b. Power peaking factors

Fig. 7. ASI and power peaking factors during the PLFO simulation.

$$x_v = \frac{h_{mix} - h_{sl}}{h_{sv} - h_{sl}}. \quad (9)$$

$$x = \frac{x_v - x_d \left[ 1 - \tanh \left( 1 - \frac{x_v}{x_d} \right) \right]}{1 - x_d \left[ 1 - \tanh \left( 1 - \frac{x_v}{x_d} \right) \right]} \text{ if } x_v \geq x_d, \quad (10)$$

$$x = 0 \text{ if } x_v < x_d. \quad (11)$$

$$x_d = -\frac{C_{pl} Z}{h_{lg}}, \quad (12)$$

$$Z = \frac{B - \sqrt{B^2 - 4AC}}{2A}, \quad (13)$$

where

$$A = 4C_B (H_{DB} + H_{HN})^2, \quad (14)$$

$$B = 2H_{DB}^2 (H_{HN} + 0.5H_{DB}) + 8q'' C_B (H_{HN} + H_{DB}), \quad (15)$$

$$C = 4C_B q''^2 + q'' H_{DB}^2, \quad (16)$$

$$H_{HN} = 0.2 \text{Re}_l^{0.662} \text{Pr}_l K_l / D_h, \quad (17)$$

$$C_B = 0.05358 e^{P/630}, \quad (18)$$

$$H_{DB} = 0.023 \text{Re}_l^{0.8} \text{Pr}_l^{0.4} K_l / D_h. \quad (19)$$

$$q''_{\text{thom}} = C_B (T_w - T_{\text{sat}})^2. \quad (20)$$

$$q''_{\text{thom}} + H_{DB} (T_w - T_{\text{sat}}) + H_{DB} (T_{\text{sat}} - T_{\text{bulk}}) - q'' = 0. \quad (21)$$

$$f = \frac{64}{\text{Re}} \text{ if } 0 < \text{Re} \leq 2320. \quad (22)$$

$$f = \frac{0.3164}{\text{Re}^{0.25}} \text{ if } 2320 < \text{Re} \leq 30,000. \quad (23)$$

$$f = \frac{0.184}{\text{Re}^{0.20}} \text{ if } 30,000 < \text{Re} \leq 1,000,000. \quad (24)$$

$$\xi^2 = \frac{(1-x)^2}{(1-\alpha)^{1.42}} \text{ if } 0 < \alpha < 0.6. \quad (25)$$

$$\xi^2 = 0.478 \frac{(1-x)^2}{(1-\alpha)^{2.2}} \text{ if } 0.6 < \alpha < 0.9. \quad (26)$$

$$\xi^2 = 1.73 \frac{(1-x)^2}{(1-\alpha)^{1.64}} \text{ if } 0.9 < \alpha < 1.0. \quad (27)$$

$$\alpha = \frac{x(0.833 + 0.167x)}{(1-x)R + x} \text{ with } R = \frac{v_l}{v_v}. \quad (28)$$

Currently, the ATOM reactor design is still in the stage of design optimization. For this study, major design parameters in Table 1 are

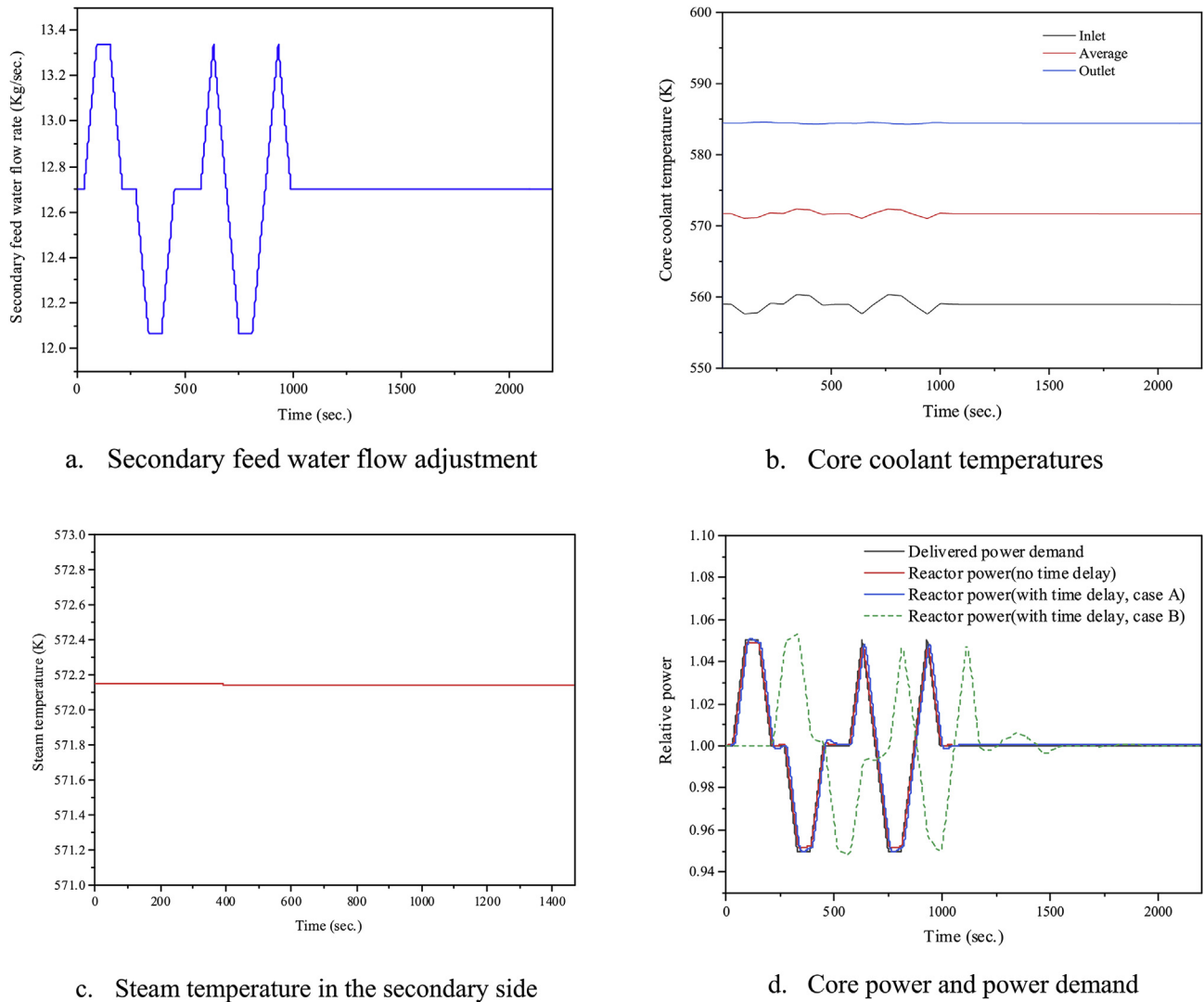


Fig. 8. PAFO simulation performed by 3-D core multi-physics coupled with HCSG module.

assumed for the HCSG modelling. It also shows a few design parameters of the ATOM core.

### 3. Results and discussions

In this section, we perform numerical simulations of the passively autonomous power maneuvering in the SBF 450 MW<sub>th</sub> ATOM SMR. As shown in Fig. 1, the core outlet coolant enters the primary of the HCSG after certain time delays, i.e., the time delay on the hot leg ( $\tau_{dh}$ ). In Fig. 1,  $T_i$  and  $T_e$  stand for core inlet and outlet coolant temperatures, respectively, and  $T_{hi}$  and  $T_{ho}$  indicate respectively temperatures of the inlet and outlet coolant of the HCSG primary side. It should be recalled that the feedwater flow rate to the secondary side of the HCSG is adjusted to extract the demanded power from the primary loop. Thermal-hydraulic simulations in both the primary and the secondary sides of the HCSG are performed, and they are coupled with the NEM-based core multi-physics simulation. The outlet coolant from the HCSG primary enters the reactor core after certain time delays, i.e., the time delay on the core cold leg ( $\tau_{dc}$ ).

#### 3.1. PLFO with helical-coil steam generator

The investigated passively autonomous load-follow scenario is a 100-50-100 power maneuvering with power ramping speed of 5% of the rated power per minute. The simulations are carried out at BOC when CTC is least negative in the fuel cycle [5]. Fig. 6-a shows the adjustment of the feedwater flow rate to the HCSG secondary side to extract the demanded power. Extracting the demanded power from the primary loop varies  $T_i$ , as shown in Fig. 6-b. In this figure, 8 s of an augmented time-delay is assumed rather arbitrarily. The augmented time delay represents the total coolant time delay on both the cold and the hot legs and the other various system components. Fig. 6-b also shows that the deviations of core average coolant temperature are rather limited although they are beyond the typical coolant temperature dead-band. Therefore, a widened dead-band is required in ATOM for the passively autonomous daily load-follow operation. It is worthwhile to note that  $T_e$  is affected by two competing parameters,  $T_i$  and fuel temperature, and limiting the variation of the  $T_e$ . An increase of  $T_i$  will decrease the reactor power and therefore the fuel temperature should decrease, due to the negative CTC, and vice versa. Fig. 6-c illustrates that the steam temperature in the secondary of the HCSG is almost constant



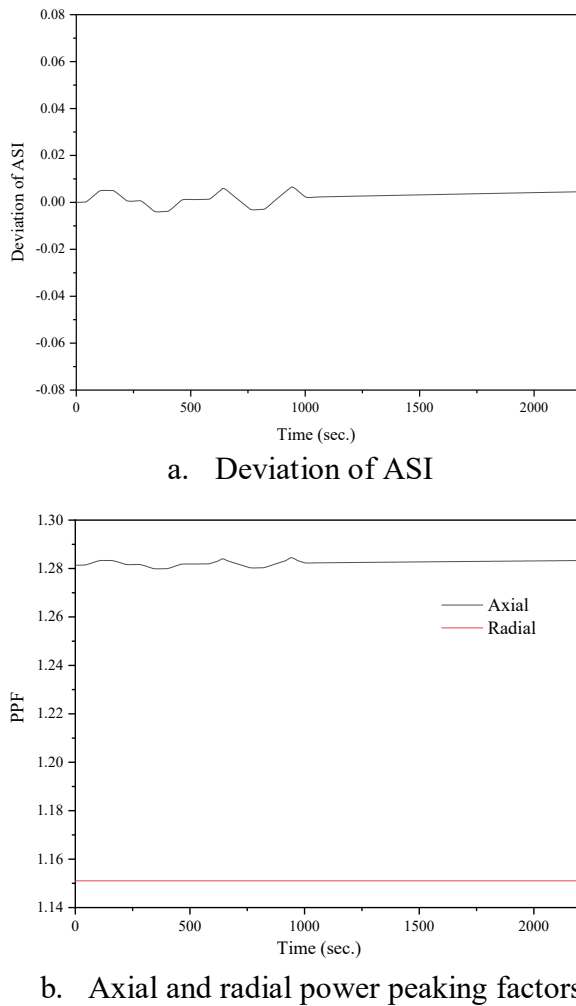


Fig. 9. ASI and power peaking factors during the PAFO simulation.

during the passive power transients. In addition, Fig. 6-d shows the core power variation due to the variation of  $T_i$ . In Fig. 6-d, we also perform a sensitivity analysis on the augmented system time delay. Cases A and B stand for 8 s and 100 s augmented system time-delay, respectively. The core power follows well the power demand due to the strongly negative CTC, especially for case A. Case B is a rather extreme case to study the impact of a big coolant time delay on the passive core power response during the PLFO. It was found that the time delay mainly delays restoration of the energy balance between the primary and secondary loops. Meanwhile, Fig. 7 shows small variations of the axial shape index (ASI) and the assembly-wise power peaking factors (PPF), in radial and axial directions, during the PLFO with case A. It is worthwhile to mention that a wide ASI dead-band can be used in ATOM SMR because there is no concern of Xe oscillations due to the relatively small dimensions of the core. The deviation of  $T_i$  is radially uniform, and thus the radial PPF remains almost unchanged during the passive power transients. However, the axial power peaking factor undergoes small variations during the PLFO since the axial power shape changes noticeably, as indicated in the ASI plot.

### 3.2. PAFO with helical-coil steam generator

This section shows the results of a passively autonomous

frequency control operation (PAFO). The scenario considered is a secondary (or remote) frequency control operation. In this operational mode, the range of power maneuvering is narrow, i.e.,  $\pm 5\%$  of the rated power, with high power ramping rate of 5%/min. Fig. 8 shows the variations of the secondary feedwater flow rate, the core coolant temperatures, the steam temperature in the secondary side, and the core power plotted together with the power demand. It is clear from Fig. 8-b that deviations of  $T_i$  and  $T_e$  are sufficiently small. In addition, the deviations of the core average coolant temperature are within the conventional coolant temperature dead-band. Fig. 8-c illustrates that the steam temperature in the HCSG's secondary side is constant during the PAFO. In Fig. 8-d, Case A stands for 8 s of augmented system time-delay, while case B is an extreme case of 200 s augmented system time delay. The core power follows well the power demand for case A. While, for case B, the assumed big system time delay leads to a delay in the core power response to the power demand variation and a slower restoration of the energy balance between the primary and the secondary loops. In case B, apart from such delayed core response, the core power follows the magnitude and the speed of the demanded power variation. In general, the system time-delay should be minimized for a better balance between the energy generated in the primary loop and the energy consumed in the secondary loop. Moreover, Fig. 9 illustrates sufficiently small deviations of the ASI and the assembly-wise power peaking factors during the PAFO.

## 4. Conclusions

A time-dependent helical-coil steam generator (HCSG) model has been coupled with 3-D transient and thermal-hydraulic coupled whole core calculations to investigate the feasibility of the passively autonomous power maneuvering without control rods or soluble-boron. The study is carried out for both a 100-50-100 daily load-follow and secondary frequency control operations in the 450 MW<sub>th</sub> ATOM system model.

In the secondary loop, the feedwater flow rate is adjusted to extract the required power demand from the primary loop. The numerical simulations show almost unchanging steam temperature in the HCSG's secondary which reflects a favorable safety feature in the secondary loop. In the primary loop, due to the variation of the amount of heat transferred to the secondary loop, the core inlet coolant temperature will inversely change with the power demand variation. Meanwhile, due to the clearly negative coolant temperature coefficient in the SBF core, the core power variation follows well the power demand variation. The core outlet coolant temperature is affected by two competing parameters: the core inlet coolant temperature and the fuel temperature. These two parameters will always oppose each other during the passive power transients. Consequently, this phenomenon limits the variation of the core exit coolant temperature during the passive power transients. For the passively autonomous load-follow, it was found that a little wider coolant temperature dead-band than that used in conventional PWRs is required. The deviations of the axial shape index and the axial and radial power peaking factors are found sufficiently small. For the passively autonomous frequency control operation, the variations of the core average coolant temperature are always within the conventional dead-band. In addition, the axial shape index and the axial and radial power peaking factors are very small.

## Declaration of competing interest

The authors declare that they have no known competing financial interests or personal relationships that could have appeared to influence the work reported in this paper.

## Acknowledgements

The National Research Foundation of Korea (NRF) Grant funded by the Korean Government (MSIP) (NRF-2016R1A5A1013919) supported this work.

## References

- [1] A. Lokhov, Technical and Economic Aspects of Load Following with Nuclear Power Plants, NEA, OECD, Paris, France, 2011.
- [2] A.A.E. Abdelhameed, J. Lee, Y. Kim, Physics conditions of passive autonomous frequency control operation in conventional large-size PWRs, *Prog. Nucl. Energy* 118 (2020) 103072.
- [3] Y.-H. Kim, et al., Load follow performance of KNGR using an extended mode-K control logic, in: *Proceedings of the Korean Nuclear Society Conference*, Korean Nuclear Society, 1999.
- [4] S.-Y. Oh, et al., Mode K—a core control logic for enhanced load-follow operations of a pressurized water reactor, *Nucl. Technol.* 134 (2) (2001) 196–207.
- [5] A.A.E. Abdelhameed, et al., Feasibility of passive autonomous frequency control operation in a Soluble-Boron-Free small PWR, *Ann. Nucl. Energy* 116 (2018) 319–333.
- [6] X.H. Nguyen, C. Kim, Y. Kim, An advanced core design for a soluble-boron-free small modular reactor ATOM with centrally-shielded burnable absorber, *Nuclear Engineering and Technology* 51 (2) (2019) 369–376.
- [7] A.A.E. Abdelhameed, Y. Kim, Three-dimensional simulation of passive frequency regulations in the soluble-boron-free SMR ATOM, *Nuclear Engineering and Design*, 2020, p. 110505.
- [8] J. Leppänen, *Serpent—a Continuous-Energy Monte Carlo Reactor Physics Burnup Calculation Code*, vol. 4, VTT Technical Research Centre of Finland, 2013.
- [9] B. Christensen, Three-dimensional static and dynamic reactor calculations by the nodal expansion method, Risoe National Lab, 1985.
- [10] S. Dulla, E.H. Mund, P. Ravetto, The quasi-static method revisited, *Prog. Nucl. Energy* 50 (8) (2008) 908–920.
- [11] Y. Jo, B. Cho, N.Z. Cho, Nuclear reactor transient analysis by continuous-energy Monte Carlo calculation based on predictor-corrector quasi-static method, *Nucl. Sci. Eng.* 183 (2) (2016) 229–246.
- [12] K.S. Chaudri, J. Kim, Y. Kim, Development and validation of a fast sub-channel code for LWR multi-physics analyses, *Nuclear Engineering and Technology*, 2019.
- [13] E. Brega, E. Salina, COBRA-EN, Thermal-Hydraulic Transient Analysis of Reactor Cores, 2001.